Martínez-Mateu, L.; Romero Pérez, L.; Saiz Rodríguez, FJ.; Berenfeld, O. (2019). Far-field contributions in multi-electrodes atrial recordings blur distinction between anatomical and functional reentries and may cause imaginary phase singularities A computational study. Computers in Biology and Medicine. 108:276-287. https://doi.org/10.1016/j.compbiomed.2019.02.022

Manuscript submitted to the special issue of:
Computers in Biology and Medicine
Quantitative Cardiology Symposium II

Far-Field Contributions in Multi-Electrodes Atrial Recordings Blur Distinction between Anatomical and Functional Reentries and May Cause Imaginary Phase Singularities – A Computational Study

Authors:

Laura Martínez-Mateu[1], Lucía Romero[1], Javier Saiz[1] and Omer Berenfeld[2]

Affiliations:

[1] Centro de Investigación e Innovación en Bioingeniería, Universitat Politècnica de València, Valencia, Spain

[2] Center for Arrhythmia Research, University of Michigan, Ann Arbor, Michigan, USA

Corresponding author:

Laura Martínez-Mateu
E-mail: laumarma@ci2b.upv.es (LM)
Phone: +34 963877007 Ext: 67030

[¶]JS and OB share senior authorship

ABSTRACT

Background: Atrial fibrillation (AF) is the most common cardiac arrhythmia and the most important cause of embolic stroke, requiring new technologies for its better understanding and therapies. Recent approaches to map the electrical activity during AF with multi-electrode systems aim at localizing patient-specific ablation targets of reentrant patterns. However, there is a critical need to determine the accuracy of those mapping systems. We performed computer simulations as a numerical approach of systematically evaluating the influence of far-field sources on the electrical recordings and detection of rotors. **Methods:** We constructed 2 computer models of atrial tissue: (i) a 2D sheet model with varying non-active cells area in its center, and (ii) a whole realistic 3D atrial model. Phase maps were built based on the Hilbert transform of the unipolar electrograms recorded by virtual 2D and 3D multi-electrode systems and rotors were tracked through phase singularities detections. **Results:** Analysis of electrograms recorded away from the 2D atrial model shows that the larger the distance between an electrode and the tissue model, the stronger the far-field sources contribution to the electrogram is. Importantly, even if an electrode is positioned in contact with the tissue, the electrogram contains significant contributions from distal sources that blur the distinction between anatomical and functional reentries. Moreover, when mapping the 3D atrial model, remote activity generated false phase singularities at locations without local reentrant excitation patterns. **Conclusions:** Far-field contributions to electrograms during AF reduce the accuracy of detecting and interpreting reentrant activity.

Keywords

Mapping, Electrogram, Phase analysis, Far-field, Rotors, Reentry

Funding

This work was supported in part by Programa Prometeu de la Conselleria d'Educació, Formació I Ocupació de la Generalitat Valenciana, award number PROMETEU/2016/088; Plan Estatal de Investigación Científica y Técnica y de Innovación 2013-2016 del Ministerio de Economía, Industria y Competitividad of Spain, Agencia Estatal de Investigación and the European Commission (European Regional Development Funds - ERDF -FEDER), award number DPI2016-75799-R; The National Heart, Lung, and Blood Institute grant R01-HL118304; the Gelman Award from the Cardiovascular Division at the University of Michigan; and the Coulter Program Award from the Dept. of Biomed Eng. at the University of Michigan.

Conflict of Interests

OB received research support from Medtronic, St. Jude Medical and Abbott. He is a cofounder and Scientific Officer of Rhythm Solutions, Inc., Research and Development Director for S.A.S. Volta Medical and consultant to Acutus Medical. None of these entities was involved in this study.

1. INTRODUCTION

Cardiovascular diseases are responsible for approximately 17 million deaths per year around the world (31% of the major causes of death). Among them, cardiac arrhythmias, i.e. disorders of the electrical conduction system of the heart, can be life threatening and cause medical emergencies[1]. Atrial fibrillation (AF) is the most common cardiac arrhythmia seen in clinical practice and is the most important cause of embolic stroke[2,3]. Its prevalence increases with aging population and increased comorbidities. In 2015 there were about 33 million people with AF worldwide[4] and it is predicted that in 2030 between 14 and 17 million people will suffer AF in the European Union alone[5]. Therefore, it is of vital importance to develop new technologies aimed at diagnosing and terminating AF and among others, computational models are a valuable and helpful tool that can play an important role in the development and validation of those technologies.

Catheter ablation has been recently recommended as a first-line treatment for AF termination[5] since it has been demonstrated to be superior to antiarrhythmic therapy for the maintenance of sinus rhythm (SR)[6–8]. Traditionally, ablation procedures aimed at terminating AF have been primarily focused on isolating the pulmonary veins (PV)[9–11] and often complemented by linear ablation of the posterior left atrium (LA)[12]. In contrast, recent approaches motivated by experimental optical mapping of animal models[13–16] and explanted human hearts[17,18], are based on mapping electrical activity and target the patient-specific AF drivers across the entire atria, being either focal or rotors and regardless of their anatomical position[19,20]. However, clinical AF mapping approaches utilize relatively low resolution multi-electrode systems (contact and non-contact)[19,21–27] lacking rigorous validation against the experimental optical mapping. Although the panoramic contact multi-electrode basket catheters to map the atria in search for AF drivers has been reported to enable >80% success

rates as compared to 20-50% obtained by conventional ablation[2,21,28], the hypothesis of rotors as human AF drivers is still controversial[24,25,29–35] and the usage of the multi-electrode mapping approach to target those drivers needs further studies to determine its accuracy.

Some of the drawbacks of the multi-electrode systems might be the lack of direct contact and a distance between a given electrode and the atrial tissue, the effect of far field sources on the recordings and the interpolation of the signals to improve maps visualization[36,37]. In the case of the mapping with a basket type of catheter, it is also common to observe splines' bunching resulting in an unpredictable and non-uniform inter-splines space compromising the panoramic coverage[38]. Here we utilize computer simulations to overcome clinical and experimental limitations in studying factors affecting the accuracy of multi-electrode mapping and focus on the influence of atrial far-field sources on the detection of rotors. We find that far-field contributions of atrial electrical sources might blur the distinction between functional and anatomical reentries, and may form false rotors on phase maps due to the inherent sensitivity of the phase analysis to low amplitude signals, which is critical in studying rotors[36,39].

2. COMPUTATIONAL METHODS

2.1 Atrial Cells and Geometrical Models

The membrane electrical activity of a human atrial myocyte was simulated with the Courtemanche-Ramirez-Nattel (CRN) ionic model[40]. The CRN model was modified to account for the remodeling of atrial cells under paroxysmal AF (pAF) and chronic AF (cAF) conditions[36,39]. The maximum conductance of different ionic channels in the cellular models was also modified to reflect the atrial electrophysiological heterogeneity observed experimentally[36] and generate action potentials (APs) as shown in Figure 1.

Cellular models were then incorporated into nodes of two atrial geometrical models: a mesh corresponding to a 2D virtual sheet of atrial tissue and a mesh corresponding to a whole 3D virtual atrial model (referred to as 2D and 3D models). The 2D model consisted of atrial cells on a rectilinear 5×5 cm^2 active nodes mesh (inter-nodal distance of 300 μm), representing atrial tissue, and a coupled cube of passive nodes, representing the blood cavity. Simulations were carried out on three versions of such 2D geometry: A uniform mesh, as well as meshes with passive nodes in a small and large central circular area representing the pulmonary vein (PV) and the mitral valve ring (MVR) atrial orifices, respectively. The 3D atrial model comprised of atrial cells in 754893 nodes and 515010 hexahedral elements with a regular spatial resolution of 300 μm, and a wall thickness between 600 and 900 μm [36].

2.2 Action Potential Propagation and Electrograms

The transmembrane APs were simulated on the cellular meshes and then the extracellular potentials were calculated on the endocardial surface and on virtual multi-electrode systems in two general steps: First the APs were solved by the monodomain formulation using the operator splitting numerical scheme with ELVIRA software[41] with a constant time step of 0.01 ms. Second, extracellular potentials were computed by an approximation of the bidomain formulation in two additional steps[42] implemented in MATLAB (MathWorks, Natick, MA) with custom-made software routines with a temporal resolution of 1 ms, and yielded unipolar electrograms (EGMs).

The detailed calculation approach follows. The bidomain equations can be partially decoupled when assuming equal anisotropy ratios for the intracellular (D_i) and extracellular (D_e) conductance tensors, i.e. $D_e=\lambda D_i$. As a result, we obtain two different equations in the heart domain describing the changes in the transmembrane potential (V_m) and the extracellular potential (V_e) [43]:

$$\nabla \cdot (D\nabla V_m) = C_m \cdot \frac{\partial V_m}{\partial t} + I_{ion} \text{ in } \Omega_H \quad (1)$$

$$\nabla \cdot (D\nabla V_e) = -\frac{1}{1+\lambda} \nabla \cdot (D\nabla V_m) \text{ in } \Omega_H . \quad (2)$$

$D = \frac{\lambda}{1+\lambda} D_i$ is the equivalent conductivity tensor, I_{ion} and C_m are the transmembrane ionic current and the membrane capacitance from the cellular model, respectively, and Ω_H is the heart domain. Equations (1) and (2) are subjected to the following boundary conditions:

$$n \cdot (D\nabla V_m) = 0 \text{ on } \partial\Omega_H \quad (3)$$

$$n \cdot (D\nabla V_e) = 0 \text{ on } \partial\Omega_H , \quad (4)$$

n being the outward normal to $\partial\Omega_H$. The two-step solution for the extracellular potential consisted of computing first V_m through equations (1) and (3), and then computing V_e in the heart tissue via equations (2) and (4). As boundary conditions (3) and (4) consider the heart to be immersed in a non-conducting bath, accurate calculation of the EGMs in the inner atrial blood cavity require placing the heart within the torso and solving for V_e within the entire domain; i.e., within the heart region, Ω_H, and the torso region, Ω_T. Therefore, the problem included now the governing equations for the solid volume conductor associated with the torso together with its boundary conditions at the heart-torso (in the 3D model) or heart-blood (in the 2D model) interface, $\partial\Omega_H$. Under the assumption of equal anisotropy ratio for D_i and D_e and following the calculation of V_m, V_e was calculated within the domain $\Omega_H \cup \Omega_T$ as the solution of the following Laplace equation:

$$\nabla \cdot (D_T \nabla V_T) = 0 \quad \text{in} \quad \Omega_T \quad (5)$$

where V_T and D_T are respectively the extracellular potential and the heterogeneous conductance tensor outside of the heart domain (including the blood cavity of the atria and the torso domains). Equation (5) is subjected to the following boundary and continuity conditions:

$$V_e = V_T \quad \text{on} \quad \partial\Omega_H \tag{6}$$

$$n \cdot (D\nabla V_T) = 0 \quad \text{on} \quad \partial\Omega_T \tag{7}$$

where $\partial\Omega_T$ is the boundary corresponding to the torso-air or the blood-air approximation for the 3D or 2D models, respectively. Finally, the computed V_T is the EGM at any virtual electrode location within the corresponding Ω_T.

2.3 Transmembrane and EGM Voltage Analysis

The time-series of the EGMs voltage values at the multiple virtual electrode locations were spatially interpolated and the Hilbert transform (HT) was applied on all the resulting voltage time series[14,44,45] to generate the instantaneous local phases, whose values ranged from −π to π radians. Finally, to track the pivoting location of the waves[46–49], phase singularity (PS) points were identified automatically by the method proposed by Rogers[50]. We excluded the first and last 500 ms of the signals to avoid transformation artifacts. It should be noted that EGMs were computed at virtual multi-electrode systems, i.e. electrodes corresponded to a spatial coordinate.

3. MAPPING OF THE ELECTRICAL ACTIVITY IN A VIRTUAL SHEET OF ATRIAL TISSUE

3.1 Near and Far field Contributions

A simulation of a planar AP wave in a 2D virtual sheet of left atrial tissue (LA_{tissue}) was performed for a baseline analysis of the relative influences of near-field (NF) and far-field (FF) sources on EGMs. An electrode was placed at a varying distance d above the center of the sheet (Figure 2A) which was arbitrarily divided into a disc of radius r comprising the designated NF sources and the periphery of the disc comprising the designated FF sources (Figure 2B). The radius r of the disc ranged from 0.25 to 2 cm to vary the extension of the sources considered as NF contribution to the EGM. For each of the NF-FF configurations of the tissue model and for all the EGM

electrode distances d, the EGMs were computed accounting for either only for the NF sources (EGM_{NF}) or for the entire LA_{tissue} with the aim of comparing the relative contributions. Results are illustrated in Figure 3. First, panel A shows endocardial EGMs, computed at d=0 with the whole tissue and with only the NF sources as designated by r=0.25 cm and r=0.50 cm (green circles in the inset). It is seen that the negative slope indicating the activation time is consistent for the 3 EGMs, but the peak-to-peak amplitude is slightly different and the area under the whole tissue EGM is significantly larger than the NF EGMs, highlighting that an electrode positioned in contact to the tissue contain significant contributions from distant areas.

To quantify the relative contribution of NF to the EGMs we compared the peak-to-peak amplitude ratio between the EGM from the NF sources (A_{ppNF}) and the whole tissue EGM (A_{pp}) amplitude (panel B), and the correlation between the EGM from the NF sources (EGM_{NF}) and the whole tissue EGM (panel C), at the same electrode position and increasing heights as well as larger NF sources area. For all values of r, the contribution of the NF sources to the whole signal decreased with the distance to the tissue (a decrease in A_{ppNF}/A_{pp} and correlation values can be observed), which means that the relative FF sources contribution increased with d. Panel D depicts, based on the data in panels B and C, the minimal size of NF region monitored by and electrode at a certain distance which yields the 90% A_{ppNF}/A_{pp} and 0.9 NF and NF+FF correlation (black dashed lines in B and C). Noticeably, increasing the distance between the electrode and the tissue increases the radius r of the region contributing 90% to the EGMs. When the electrode was located at a distance of 19.8 mm from the endocardium, none of the tested radii yielded the 90% of A_{ppNF}/A_{pp}. Overall, as expected, the higher the distance between an electrode and the tissue, the stronger the FF sources contribution to the EGM in that electrode is. This fact will reduce fidelity in interpretation of unknown patterns of waves, for example during fibrillation, in which remote waves contributions may interfere with local waves contributions.

3.2 Mapping Reentries by using Multi-Electrode Arrays

A simulation of reentrant activity was performed in the LA_{tissue} under pAF conditions to characterize the effects of the multi-electrode array configurations, including variations in both the inter-electrode distance (d_{ie}) and the electrode-to-tissue distance d, on the accuracy of localizing rotors and their meandering. In addition, a couple of anatomical reentries were performed around a pulmonary vein (PV) and the mitral valve ring (MVR) to test whether using multi-electrode array systems can distinguish between anatomical and functional reentries. For this purpose, unipolar EGMs were computed at the endocardium and at the coordinates where the electrodes were located within the blood cavity. Then the voltages on the EGMs were linearly interpolated to 0.3 mm of spatial resolution to obtain a uniform visualization of the phase maps and the PSs.

3.2.1 Accuracy of the Multi-electrode Arrays Configuration

We altered multi-electrode array configurations to analyze rotor detection by varying d from 0.9 mm to 19.8 mm and d_{ie} from 0.9 mm to 18 mm (see Figure 4). Results are summarized in Figure 5. Phase maps and rotor tracking are shown for each multi-electrode array configuration, in comparison with those obtained at the endocardium (our ground-true reference). Rotor was tracked through the PSs detection for each multi-electrode array configuration [50]. Sensitivity and specificity were calculated by comparing the trajectories detected by each multi-electrode array configuration and the trajectory detected on the endocardium. As expected, phase maps of the multi-electrode array configuration with the minimal $d=d_{ie}=0.9$ mm are the ones that resemble most the endocardial phase map and that yield the most accurate trajectory detection with a sensitivity of 85.7% (see Figure 5). Increasing d decreased the sensitivity (31.4% at d=19.8 mm.) Surprisingly, the effects of increasing d_{ie} on the phase maps seem to be stronger when the electrode is closer to the tissue (smaller d). By increasing d, sensibility improved probably

because of altered balance between near and far filed contribution (from 5.9% to 20.3% for the highest d_{ie}=18 mm). Although specificity was greater than 84% in all cases, it also decreased by increasing d and d_{ie} from a maximum of 99.2% at d=d_{ie}=0.9 mm.

3.2.2 Differentiation Between Functional and Anatomical Reentries

We used the simulation of the functional reentry in the LA_{tissue} in Figure 5 and simulation of an anatomical reentry around a PV (PV_{tissue}) and the MVR (MVR_{tissue}) models under pAF conditions to investigate the ability of multi-electrode arrays to distinguish between functional and anatomical reentries in Figure 6. The multi-electrode array configuration employed in this case corresponds to d_{ie}=0.9 mm at the endocardial surface (d=0 mm) since, as described previously, it provides the best functional reentry (rotor) detection.

An S1-S2 cross-field stimulation protocol yielded reentries in the three different models, as shown in Figure 6 (column 1, 2 and 3 correspond to simulations in the LA_{tissue}, PV_{tissue} and MVR_{tissue}, respectively). Panel A depicts snapshots of the V_m (multi-electrode arrays are represented as superimposed grid of black dots). Panel B shows maps of peak to peak amplitude over a full cycle of V_m and illustrates the low amplitude regions in the meandering area of the functional reentry (panel B1) and the null V_m in the orifices regions around which the anatomical reentry revolves. Panel C shows phase maps based on the simulated V_m time series at the same instant shown in panel A. For the functional reentry in the LA, the PS trajectory has been superimposed (white trace in panel C1). For the anatomical reentries, it is noticeable that PSs do not exist as the phases of the V_m do not converge to a point. Panels D and E show the EGM maps corresponding to the recordings of the multi-electrode arrays. Panel F illustrates the 1-cycle peak to peak amplitude maps from the EGMs (rotor trajectories during this cycle have been superimposed in red). Here again, as in Panel B, the area at the center of the functional reentry shows low amplitude in the EGM, but in contrast to panel B, here the anatomical reentries are

exhibiting low, but non-zero voltage. Finally, panel G depicts the phase maps based on the time-series EGMs shown in panels D-E, with PS trajectories superimposed in white.

As expected, phase maps generated by the recordings of the multi-electrode array (Panel G) exhibited the functional reentry in the LA as a rotor and its trajectory was detected through the PSs detection on the LA_{tissue} phase maps (see panel G1). However, phase maps built from the EGMs and corresponding to the anatomical reentries around the PV and the MV also displayed PSs indistinguishably from rotors (see panels G2 and G3), unlike the phase maps based on the V_m (panel C2 and C3). Noticeably, in case of both anatomical reentries, the PSs' trajectories were located inside the anatomical orifice, where there was no active tissue. This fact implies that the HT phases independency of EGMs amplitude displays rotors and PSs in extracellular potentials maps due to the far-field contribution (in this case from the surrounding active tissue). Indeed, as illustrated in panel F2-F3, the amplitude of the EGMs recorded by electrodes in contact with active tissue is much higher than the amplitude of the EGMs recorded by central electrodes which are at some distance from the active tissue (electrodes covering the orifice). Moreover, for all three reentries there is an amplitude reduction in the region of the meandering, as shown in panel F. Thus, the mere presence of a reentry and a PS in maps generated by multi-electrode recordings cannot be considered an indication for functional reentry because of the far-field contribution to the recordings and the amplitude independency of the phase analysis.

4. MAPPING ACTIVITY IN THE VIRTUAL ATRIA BY USING A BASKET CATHETER

4.1 Mapping of Reentries

We have recently demonstrated how the three main factors of (1) electrode-endocardium distance, (2) distant electrical sources and (3) inter-electrode interpolation affect the detection of rotors using a basket mapping catheter in the atria[36]. Here we build upon the insight on far-

field effects in 2D reentrant simulations shown in Figures 5 and 6 to demonstrate how distant electrical sources in an anatomically realistic model of the atria can contribute far-field extracellular potentials that affect the accuracy of reentry detection during AF. To accomplish that goal, we first simulated the reentrant electrical activity in the atria. The activation patterns of APs simulated on the atrial endocardial surface served as our ground-true reference for comparison with the basket maps. Second, we computed the unipolar EGMs on the endocardial surface and at the coordinates of a virtual intracardiac 64-pole mapping basket catheter electrodes, which was placed in the right atrium (RA), as depicted in Figure 7A. The basket catheter was formed by 8 splines (A-H) each containing 8 electrodes (1-8). Accordingly, endocardial and cavity EGMs were computed as extracellular potentials with a temporal resolution of 1 ms and were bandpass filtered (7-10 Hz) to allow a better rotor tip tracking [51]. The 64 Basket's EGMs were then linearly interpolated on 57600 points on a periodic 2D projection of the basket to improve phase maps visualization and rotor tracking (Figure 7D). Phase maps on the endocardial surface (Figure 7C) and on the basket sphere (Figure 7E) were then calculated from the filtered EGMs by applying the HT and the resulted PSs were localized on the phase maps to track the rotor's trajectory.

The performed simulation led to a self-sustained complex propagation pattern maintained by a rotor near the crista terminalis (dubbed CT rotor) accompanied by a distal rotor wave extension (RWE) reentry around the inferior vena cava (IVC). The CT rotor migrated back and forth between the superior vena cava (SVC) and the IVC along the CT. Figure 7B are snapshots at 150 ms (B1) and 1680 ms (B2) showing the CT rotor (white arrow) and the RWE (dashed white arrow). All the reentrant patterns described in the transmembrane voltage maps were also identified on the phase maps (Figure 7C). The CT rotor generated a meandering PS at the area corresponding to its endocardial V_m map pivoting and the RWE circulating around the IVC generated a stable PS inside the corresponding orifice area.

However, the phase maps of both the endocardial surface (Figure 7C) and the basket (Figure 7E) EGMs always presented a number of false rotors, dubbed imaginary PSs (IMPSs), in addition to the pair of AP simulated reentries (the CT rotor and the RWE). The IMPSs were independent of the interpolation since electrodes surrounding the IMPSs registered sequential activation and were observed in basket phase maps for each of 3 different basket positions (not shown; see [36]). Band-pass filtering employed to remove transient PSs did not eliminate IMPSs since in our simulation they appeared within the same band of frequency as the real CT rotor and RWE. False PSs consequent of interpolation between electrodes without sequential activation were also possible, but their percentage was highly reduced, or even completely removed, when electrodes density was increased (not shown, see [36]). It should be noted that the PS associated with the RWE around the IVC is not to be considered false, or imaginary, due to the fact that multi-electrode recording systems will produce a PS for both anatomical and functional reentries (see Figure 6).

For further perspective we present snapshots of the basket voltage maps at two different times in Figure 7D. The voltage scale in Figure 7D was magnified to highlight voltage distribution across the basket and indeed visual evaluation of the snapshots show voltage gradients across the basket, but those voltage gradients do not clearly indicate the real or imaginary reentrant patterns visible in the phase maps in Figure 7E. The Supplementary Movie 1 however does show the reentrant nature of the basket voltage map and corroborates the presence of the PSs in the phase maps seen in Figure 7E. It is important to emphasize that the low amplitude potentials seen in Figure 7D and Supplementary Movie 1 are not noise and cannot be filtered out without risking removing significant information across other regions of the atria during the AF.

4.2 Distal Sources Affecting Mapping

As illustrated in Figure 7C, transient PSs drift at the area corresponding to the tricuspid valve of the RA, where no voltage and reentrant activity is seen in Figure 7B. The generation of such PS in C1 can be explained by the far-field activity studied in Figure 6 (columns 2-3), where there is a similar setting containing anatomical obstacles. However, in contrast to the stable anatomical reentries around the PS in Figure 6, in Figure 7 there is no reentrant activity around the tricuspid valve ring and therefore the PS is designated IMPS.

We surmised that the origin of the IMPSs in the basket map (Figure 7E) is related to far-field contributions from remote active atrial sources. We therefore computed the endocardial and basket voltage and phase maps when considering only limited RA sources from the simulation in Figure 7 which were confined to regions away from the TV region and splines E, F and G (Figure 8A). As illustrated in panels B-D of Figure 8, IMPSs appeared at endocardial regions and between splines E-G which were clearly recording remote atrial activity. The CT rotor and its extension reentry, which were included in the sources considered, were still detected. Supplementary Movie 2 corroborates the dynamic reentrant nature of the basket voltage and phase mapping with presence of PSs and IMPSs as seen in Figure 8C and 8D.

To further determine the location of sources contributing to the presence of IMPSs we computed the endocardial and basket phase maps when considering very limited amount of sources confined to the immediate vicinity of the CT rotor core (see Figure 9A). The small area of sources generated the CT rotor and its extension reentry at the boundary of the sources region (Figure 8B), but did not generate the IMPSs at both the RA endocardial surface and the basket (compare Figure 9D with Figure 7E and Figure 8D). The basket voltage maps (Figure 9C) and Supplementary Movie 3 further corroborate the existence of low amplitude signals with rotation at sites corresponding only to the CT rotor and its extension, without IMPSs.

The fact that the sources restricted to the immediate vicinity of the CT rotor as seen in Figure 9A did not produce false or imaginary reentrant activity on the phase maps in Figure 9B and 9D is not an evidence that these region does not contribute at all to the IMPSs seen in Figures 7 and 8, but rather that the endocardial and basket IMPSs were a consequence of combined far-field contribution from sources located in various areas distal to the IMPSs. In a more detailed analysis [36] it was observed that far-field sources interfered significantly with the basket recordings when electrodes were at distances greater than about 0.5 cm from the endocardial wall activity. As the far-field effect was observed on the endocardial maps also when considering the whole atrial tissue (with short living PSs in the TV region as seen in Figure 7, panel C1) it is suggested that the far-field effect may generate false PSs even when the basket is in perfect contact with the endocardium, but the far-field effect is exacerbated when the basket electrodes are in distance >0.5 from the endocardium[36].

5. DISCUSSION

5.1 Unipolar Recording of the Electrical Activity in a Sheet of Atrial Tissue

The main contribution to a unipolar EGM in contact with the tissue in our simulation of a planar wave is provided by NF sources. Demanding that the NF to FF EGM contribution amplitude ratio is > 90% and the correlation value between the NF EGM to the NF + FF EGM is > 0.9, our study suggests that the sources considered as NF reside in a circular region of $r \geq 0.50$ cm. Then, for a NF sources region of a fixed size, the NF relative contribution to the EGM decreases by increasing the electrode-to-tissue distance and therefore, the greater the distance, the higher the relative contribution of the FF. This fact implies that at certain distances from the tissue, an electrode is recording mainly remote electrical activity. Since remote sources during fibrillation may be various and even stronger than the local ones, they might have a detrimental effect on the accuracy of mapping of wave propagation.

5.2 Mapping Reentries by using Multi-Electrode Arrays

5.2.1 Accuracy of the Multi-electrode Arrays Configuration

To establish a clear baseline understanding for localizing rotors in the whole atria, we evaluated the effects of the geometrical configuration of the multi-electrode systems on the accuracy of localizing rotors in a 2D sheet of atrial tissue by varying the multi-electrode array configurations. Simulation results in Figure 5 suggest that $d_{ie} < 9$ mm seemed to be a sufficient spatial resolution to detect rotors with a relatively high sensitivity (approximately 62 % if d_{ie}=4.5 mm, 82 % if d_{ie} = 2.7 mm and 85% if d_{ie}=0.9 mm) for low distances to the tissue (d = 0.9 mm). However, when the spatial resolution of the electrodes was poor, rotors' detection in our simulations improved by increasing the electrode-to-tissue distance d. In this study we show that the sensitivity and the specificity increase when increasing d for a resolution of d_{ie} = 9 mm or worse. These results are in accordance with a previous study that demonstrated that rotors could be detected with a spatial resolution of 1 mm to 1 cm[22]. However, we provide further insight and conclude that the minimal spatial resolution depends on the distance between the array of electrodes and the tissue.

The 2D simulation results suggest that localization of a rotor with high density multi-electrode arrays placed in a cavity parallel to a smooth endocardium can be accurate when the array is placed closest to the endocardium. For low density arrays, however, accuracy can be maintained by increasing the distance to the tissue. However, the 2D simulation results are not directly applicable to more complex atrial geometries and multi-electrode configurations with non-equidistant d_{ie}, as for example in the basket catheter, where the distance between the electrodes and the endocardium, as well as the distance to the rotor, are non-constant. Nevertheless, the data presented in Figure 5 can teach us on the 3D basket mapping in our simulations since an array placed close to the 2D atria could represent the near side of the

basket, while another array placed far from the 2D atria would represent the contralateral side of the basket. Therefore, our 2D simulations would show how the near and the contralateral aspects of the basket scenario can present PSs, either real or imaginary. The multi-electrodes array senses a PS regardless of the distance between the array and the 2D atrial model and those PSs showed at any distance from the atria in Figure 5 form filaments in the external medium, i.e., a linear collection of PSs in the extracellular potentials fields resulting from AP reentries (they are not shown in our results). A similar situation is presented by Rodrigo et al [51], where filaments of PSs exist in the torso external to the atrial wall. Those extended filaments in the cavity indeed could be a mechanism of appearance of IMPSs in the 3D simulations whereby a PS in the extracellular potential maps on the contralateral basket side and corresponding nearby atrial wall do not have a rotating action potential wave.

5.2.2 Differentiation Between Functional and Anatomical Reentry

As demonstrated in Figure 5, mapping and tracking PSs of functional reentries with multi-electrode arrays by using phase maps based on the HT of unipolar EGMs is most accurate for the minimum d_{ie} tested, as long as the array is placed as close as possible to the tissue ($d = d_{ie} = 0.9$ mm). Therefore, we used this multi-electrode array configuration to evaluate its ability to distinguish between functional and anatomical reentries.

On one hand, results showed that on both voltage and phase maps, both functional and anatomical reentries are registered by the multi-electrode array indistinguishably as a rotor, i.e. as a functional reentry. Their meandering can be detected through the PSs. In the anatomical reentries cases (Columns 2 and 3 in Figure 6) the EGM phases inside the obstacles converged and formed a PS always located within the electrodes array covering the orifice area and its meandering trajectory appeared more spatially confined compared with the meandering of the functional reentry PS. This discrepancy is probably dependent on the cellular model and also

probably due to the stabilizing effect of the orifice around which the anatomical reentry pivots. On the other hand, for both functional and anatomical reentries, there is a decrease in EGMs' amplitude in the vicinity of the detected trajectories. In the case of the anatomical reentries this decrease is due to the distance between the electrodes and the sources at the tissue (far field contributions). Unlike anatomical reentries, for the functional reentry the decrease in the EGMs' amplitude near the trajectory is a consequence of the high wave front curvature and the slow conduction velocity at the core, where the tissue remains practically unexcited[52].

5.3 Mapping of the Electrical Activity in the Virtual Atria by using a Basket Catheter

To date, the accuracy of panoramic basket catheters for localization of rotors in patients during AF has not been established, in part because the fibrillatory activation patterns across the whole atria are not known, and thus we used computer simulations to analyze in detail factors affecting localization of rotors. Our results showed that rotors may be identified by phase maps of electrical recordings. In fact, phase and voltage maps follow the same activation patterns, but due to the independency of phase analysis from the amplitude of the recordings, phase maps are more precise in detecting reentrant patterns when small potential variations in amplitude are present (see Figure 6). This could be an advantage in the case the basket catheter presents low amplitude signals either because of distance to the tissue or because of nearby scar or fibrosis. However, Figure 7 shows that phase maps built from basket catheter recordings may present imaginary PSs, which may confound targeting of ablation to terminate AF. Our analyses in Figures 6-9 and elsewhere[36] suggest that the appearance of the false rotors can be attributed to at least three factors: the distance between the basket electrodes and the endocardial wall; the distance between the atrial waves and the electrodes (these two factors are essentially a far-field effect); and the inter-electrodes distance of data used to create the maps. Therefore, although phase maps based on basket catheters are a powerful tool to map

AF and to localize real rotors and other ablative targets, they can lead physicians to ablate atrial regions that are in fact free of rotor sources of AF. Importantly, as phase and voltage maps follow the same activation patterns, this suggests that far-field effects would affect similarly the activations times and phase maps.

Our previous study suggests that an 8×8-pole mapping basket catheter can yield sufficient spatial resolution for a real rotor detection when it is properly located in contact with the tissue and at the rotor meandering area[36]. This is consistent with other mapping studies, which are not validated but include some correlations between mapping and ablation results to support their conclusions. Rappel and Narayan[22] suggested that the spatial resolution of a 64-pole mapping basket catheter is adequate to detect rotors, although noise in the EGMs and electrode position might affect accuracy. Narayan et al[19] showed that irregular inter-electrodes distances do not alter the sequential activation across adjacent electrodes surrounding a rotor.

In addition, our study showed that increasing the electrode density (e.g., 16×16) did not significantly improve rotor detection if the basket was located close to the rotor [36]. However, when we decreased the electrode density (e.g., 4×6) from an optimal level, the ability to detect rotors was reduced. Recently Roney et al[53] found that basket catheters are prone to false detections and may incorrectly render rotors that are not present, and also that increasing the number of splines up to 16 reduces both the number of false PSs and the number of missing PSs. In general, our results described here and in [36] are in accordance with their results. When we increased the number of splines up to 16, for the three basket positions the false PSs due to the interpolation were strongly reduced and the sensitivity for detection of the real rotor increased. However, our study highlights the fact that rotor tracking is more effective if the basket catheter is placed appropriately inside the atrial cavity to ensure extensive coverage of the rotor meandering area. Additionally, it is important to note that the improvement of the spatial

resolution didn't reduce the appearance of IMPSs, which were the consequence of a larger than critical electrode-to-tissue distance or far-field effect in general. Furthermore, for certain positions of the basket, the rotor would not be detected if it drifts to a poorly covered region. It should be also noted that, in the clinic, if the basket is not large enough, it would not be possible to determine if it is properly located inside a cavity because one does not know a priori the rotors' locations.

5.4 Clinical Perspective on Far Field and Mapping Reentries

In the clinical setting, the far-field activity is broadly referring to artifacts confounding the identification of local activity in unipolar or bipolar electrode recordings[54]. In certain cases, such as with the far-field contributions from the ventricles or a pacing electrode during AF recordings, the artifact is easy to identify. However, complex patterns of multiple waves during AF may produce confounding irregular far-field contributions which may vary in their cycle length, have small or large amplitudes, and are impossible to conclusively account for in all commonly used unipolar, bipolar and any reference point settings[55]. Patterns of activation have been traditionally studied with maps of presumed local activation times, but when the patterns at question are rotors, the phase mapping, which produces a similar pattern of activation as the activation times maps (compare Figures 6E and 6G), is more precise because it captures and tracks its instantaneous pivoting point, i.e., the PSs[56]. In this study we use computer simulations to demonstrate how far-field contributions of remote sources of activity in the atria can produce PSs in multi-electrode recording phase maps, which are the signature of functional reentries and rotors, in vicinity of regions which either present real functional or anatomical reentries, or regions which do not present reentries.

Reentries localized to atrial anatomical orifices, such as the valve rings or the thoracic veins, are readily categorized as anatomical reentries regardless of the erroneous presence of PS in phase

maps. However, EGMs of reentries localized to areas around a scar, fibrotic or trabeculae structure, or heterogeneity in fibers organization, which may exhibit low amplitude EGMs at baseline[55,57], could in fact be either anatomical[58] or functional[59] with different underlying physiology and possibly requiring different strategy of therapy. Our study unfortunately suggests that in the case a PS is observed on the multi-electrode maps outside of a known anatomical orifice region, it will not be possible to determine whether the PS originates from a functional or anatomical reentrant activation. Although the EGMs voltage amplitude and the meandering patterns of the PSs may be different in functional vs. anatomical reentries, the heterogeneity of these two features at different atrial sites and conditions precludes using them in a clear method to differentiate between both types of reentries[60]. Thus, until further studies are performed to establish the accuracy of multi-electrode mapping systems, an extreme caution in interpreting clinical mapping of AF waves and reentries should be applied.

6 CONCLUSIONS

Phase maps based on the HT of the unipolar EGMs registered by multi-electrode systems are capable of detecting real anatomical and functional reentries in the atria even when not in full contact with the endocardial tissue. However, as a consequence of the far-field contributions to the electrical recordings and the independency of the phase analysis from EGMs amplitudes, false reentry detection may be possible and the differentiation between functional and anatomical reentries is blurred. Future studies with the gold-standard optical mapping reference[61] will have to device in-vivo approaches to overcome such inherent limitations of the current multi-electrodes mapping systems.

508

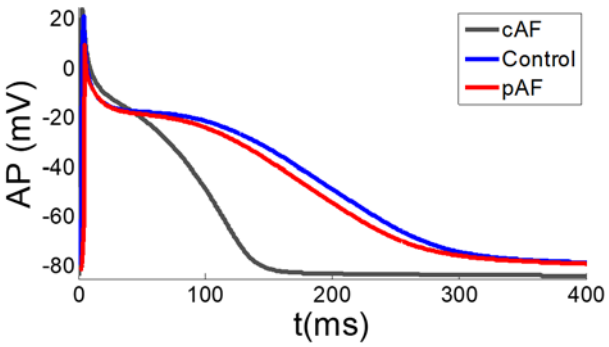

Figure 1. Action potentials (APs) in control, paroxysmal atrial fibrillation remodeling (pAF) and chronic atrial fibrillation remodeling (cAF).

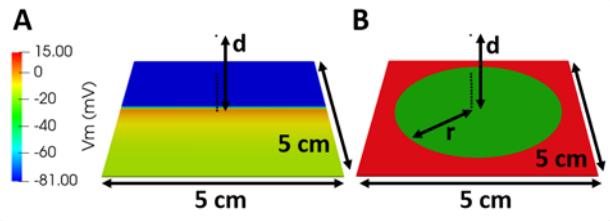

Figure 2. Far-field contributions. A) Electrical propagation in a virtual sheet of left atrial tissue (planar stimulus). B) Near-field (green) and far-field (red) regions. r: radius of the near field region, ranging from 0.25 to 2 cm; d: distance between tissue and electrode. Black dots correspond to tested positions of the electrodes.

509

510

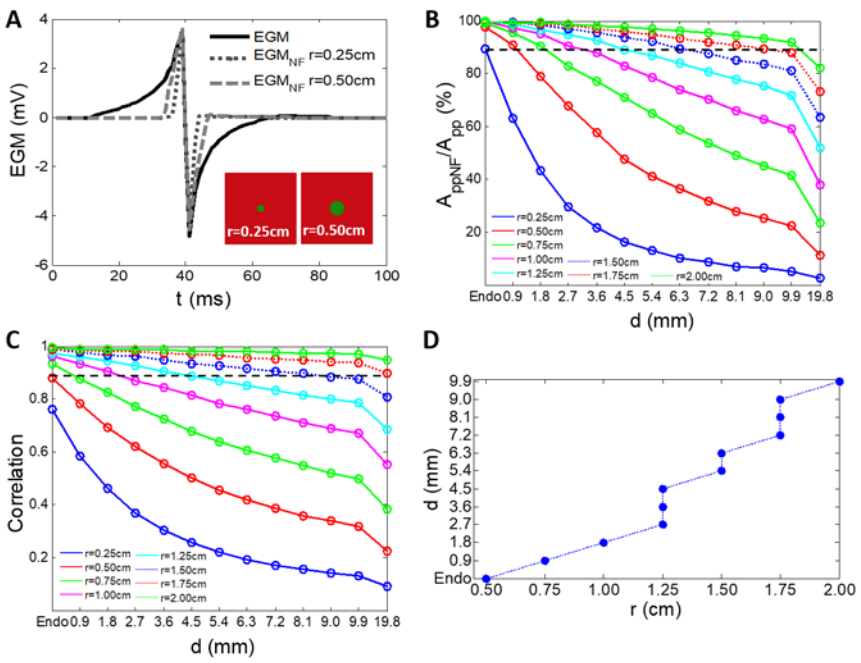

Figure 3. Near and far-field contributions. A) Comparison of the EGM and the EGM_{NF} for a near field region defined by r=0.25 and r=0.50 cm, all three registered at the endocardium. B) Ratio of the peak-to-peak amplitude (A_{pp}) and C) correlation between the EGM computed only with the NF sources (EGM_{NF}) and the EGM computed with the whole virtual atrial tissue for each electrode position and each radius r defining the NF sources. Black dashed line indicates a value of 90% in B and 0.9 in C. D) Region of tissue (radius r) covered by one electrode depending on the electrode-to-tissue distance, with 90% for the A_{ppNF}/A_{pp} and 0.9 for the correlation; Endo: d=0mm.

511

Array	d_{ie} (mm)				
d (mm)	0.9	2.7	4.5	9.0	18.0
0.9	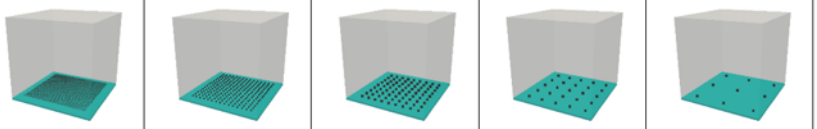				
2.7	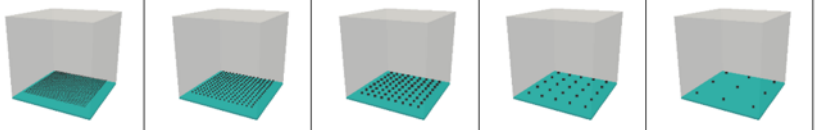				
5.4	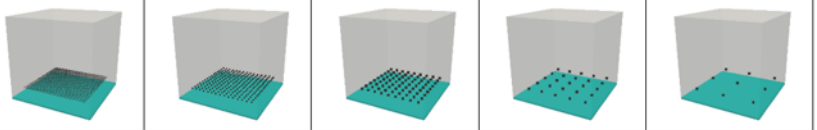				
9.9	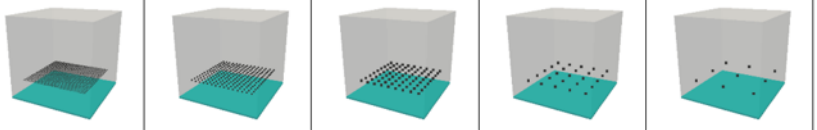				
19.8	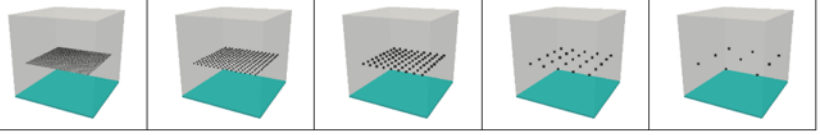				

Figure 4. Multi-electrode array configurations. The blue surface at the bottom of each panel represents the endocardial surface and the black dots represent the multi-electrodes' array. d: electrode-to-tissue distance; d_{ie}: inter-electrode distance.

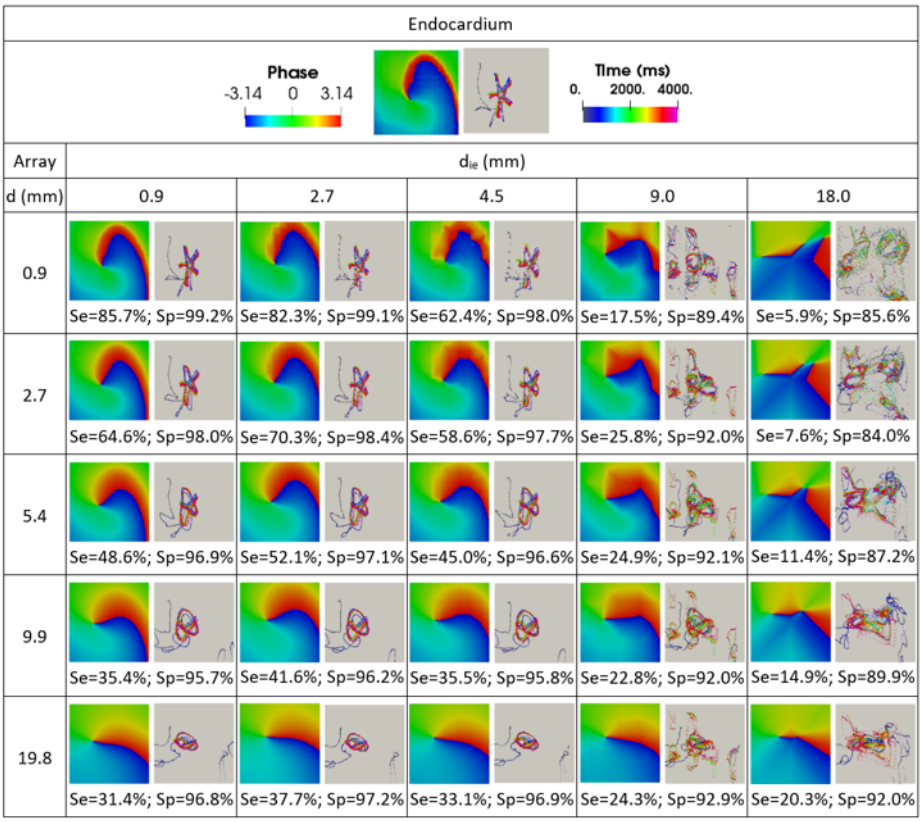

Figure 5. Multi-electrode array and rotor detection. Phase maps built based on the Hilbert transform of the linearly interpolated EGMs (left) and rotor trajectories obtained through PSs detection (right). d: electrode-to-tissue distance; d_{ie}: inter-electrode distance.

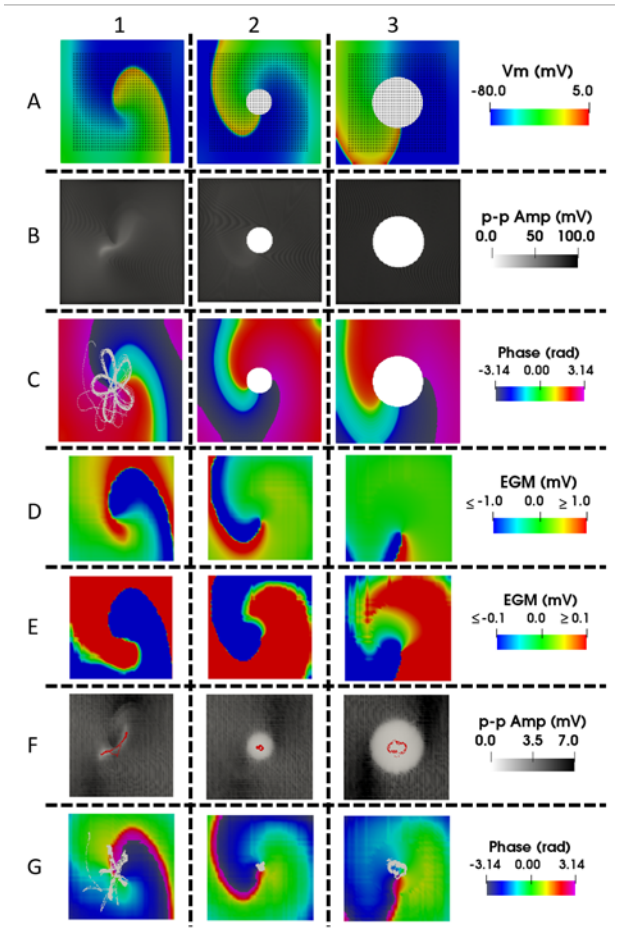

Figure 6. Simulation of functional (column 1) and anatomical (columns 2 and 3) reentries and their detection on multi-electrodes array. A) Simulated voltage maps at t=3655 ms. The grid of electrodes (black dots) is superimposed on the maps. B) Maps of 1-cycle peak to peak amplitudes of transmembrane voltage. C) Phase maps based on the simulated transmembrane voltage maps in A (trajectory of the functional reentry PS is superimposed in white in C1). D) Maps of EGMs on the electrode grid at t=3655 ms. E) Same as D, but with a magnified voltage scale. F) Maps of 1-cycle peak to peak amplitudes of EGM voltage (PS trajectories superimposed in red). G) Phase maps based on the EGMs with PS trajectories superimposed in white of functional reentry (G1) and anatomical reentries (G2 and G3). The multi-electrode array was at d=0 and d_{ie}=0.9 mm (black dots on voltage maps in A).

524

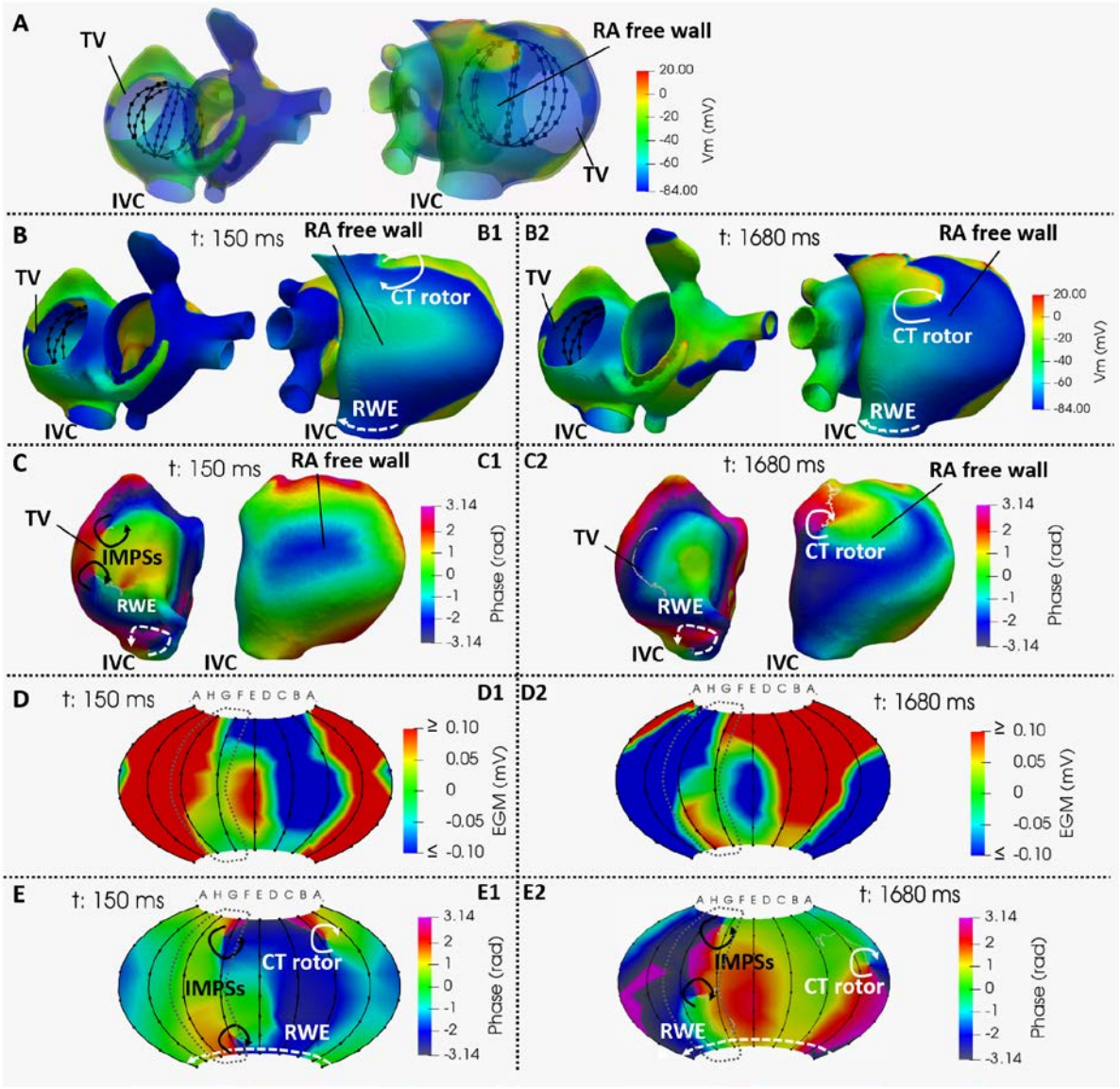

Figure 7. Mapping of the virtual RA. A) Position of the basket catheter within the virtual RA model. B) Transmembrane voltage map and reentrant propagation in the virtual atria. C) RA endocardial phase maps (CT rotor is not seen in these views at 150 ms). D) Basket voltage maps (see Supplementary Movie 1). E) Basket phase maps (dotted gray curves delimit splines covering the TV orifice). CT rotor: rotor in the crista terminalis area; RWE: rotor wave extension; IMPSs: imaginary phase singularities; IVC: inferior vena cava; TV: tricuspid valve; RA: right atrium. Arrows: reentrant patterns. Thin white lines: PSs and IMPSs trajectories.

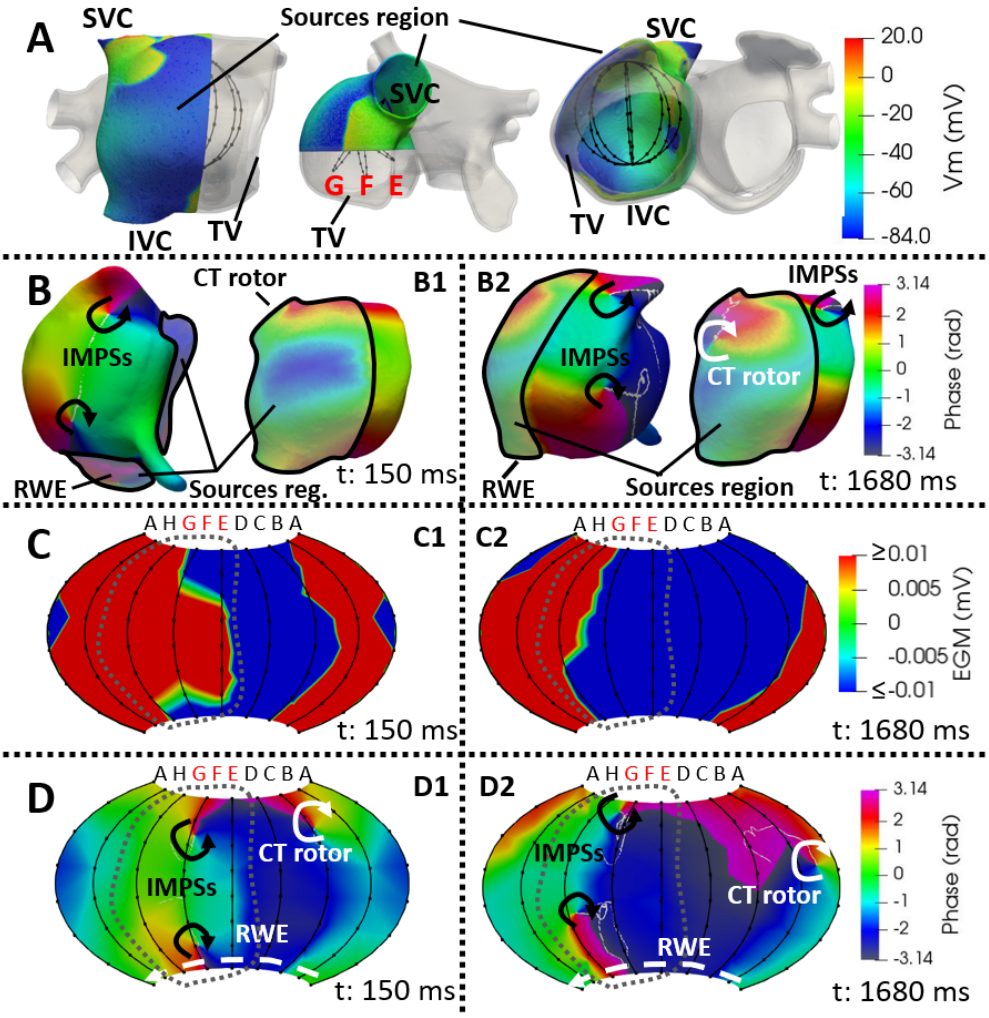

Figure 8. Mapping of the virtual RA consisting of limited sources. A) Transmembrane voltage maps of the limited sources region and position of the basket catheter. Splines G, F and E (in red) are visibly remote from the sources. B) RA endocardial phase maps at 150 ms (B1) and 1680 ms (B2) when considering the only sources illustrated in A and outlined (solid black lines designated sources region). CT rotor and RWE are not seen in these views at 150 ms and 150-1680 ms, respectively . C) Basket voltage maps at 150 ms (C1) and 1680 ms (C2) obtained when considering only the limited sources region in A (see Supplementary Movie 2). D) Basket phase maps at 150 ms (D1) and 1680 ms (D2) obtained when considering only the limited sources region in A. Dotted gray lines indicate splines located most remotely from the sources region. CT rotor: rotor along the crista terminalis; RWE: rotor wave extension; TV: tricuspid valve; SVC/IVC: superior/inferior vena cava; IMPSs: imaginary PSs. Arrows: reentrant patterns; thin white lines: PSs trajectories.

528

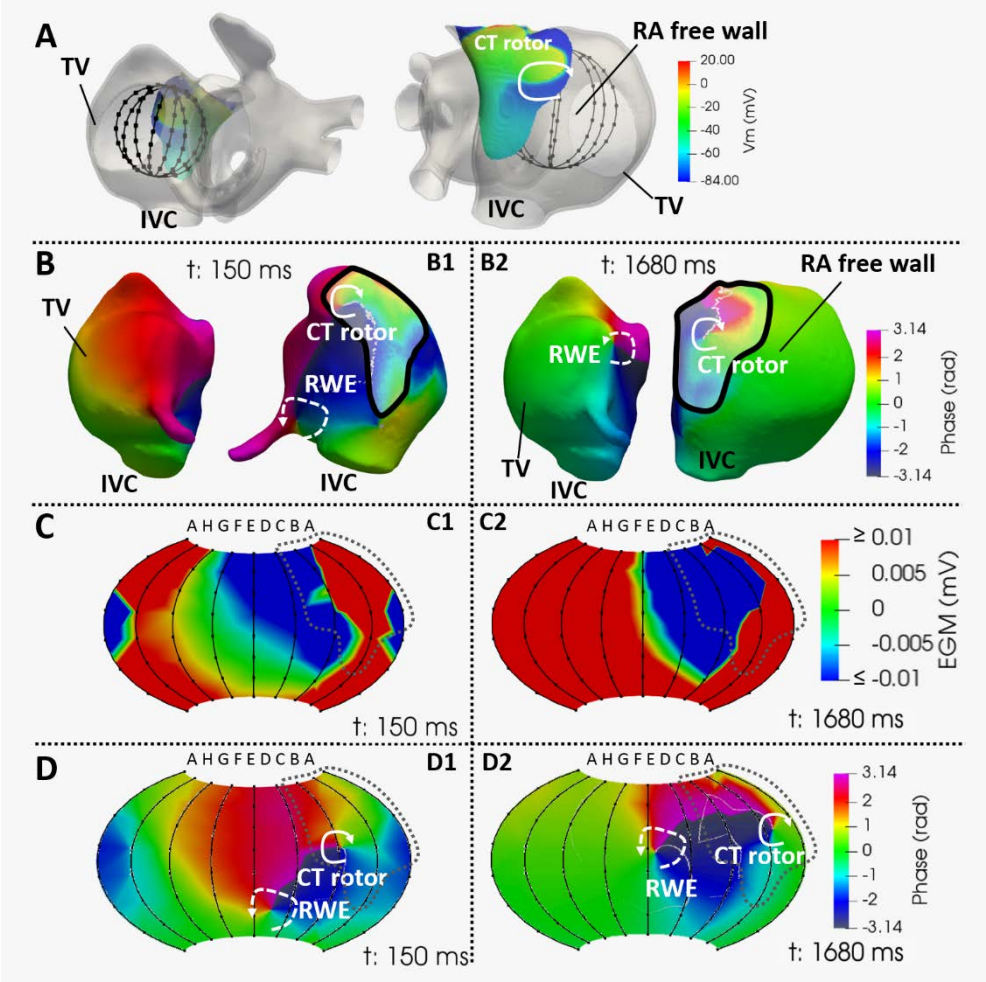

Figure 9. Mapping of the virtual RA consisting of limited sources in close vicinity of the CT rotor. A) Transmembrane voltage maps of the limited sources region and position of the basket catheter. B) RA endocardial phase maps at 150 ms (B1) and 1680 ms (B2). Solid black lines designated sources region. C) Basket voltage maps at 150 ms (C1) and 1680 ms (C2) obtained when considering only the limited sources region in A (see Supplementary Movie 3). D) Basket phase maps at 150 ms (D1) and 1680 ms (D2) obtained when considering only the limited sources region in A. Dotted gray lines indicate splines nearest to the sources region. CT rotor: rotor along the crista terminalis; RWE: rotor wave extension; TV: tricuspid valve; IVC: inferior vena cava; RA: right atrium. Arrows: reentrant patterns; Thin white lines: PSs trajectories.

Supplementary material

Movie 1: Basket maps corresponding to Figure 7. Voltage maps (left) and phase maps (right).

Movie 2: Basket maps corresponding to Figure 8. Voltage maps (left) and phase maps (right) when considering the limited sources shown in Figure 8A.

Movie 3: Basket maps corresponding to Figure 9. Voltage maps (left) and phase maps (right) when considering the limited sources in close vicinity of the CT rotor shown in Figure 9A.

552 **REFERENCES**

553 [1] S. Mendis, P. Puska, B. Norrving, Global Atlas on Cardiovascular Disease Prevention and
554 Control, World Health Organization, 2011.

555 [2] H. Calkins, K.H. Kuck, R. Cappato, J. Brugada, A.J. Camm, J. Edgerton, K. Ellenbogen,
556 M.D. Ezekowitz, D.E. Haines, 2012 HRS/EHRA/ECAS expert consensus statement on
557 catheter and surgical ablation of atrial fibrillation: recommendations for patient
558 selection, procedural techniques, patient management and follow-up, definitions,
559 endpoints, and research trial design, J. Interv. Card. Electrophysiol. 33 (2012) 171–257.
560 doi:10.1007/s10840-012-9672-7.

561 [3] C.T. January, L.S. Wann, J.S. Alpert, H. Calkins, J.E. Cigarroa, J.C. Cleveland, J.B. Conti,
562 P.T. Ellinor, M.D. Ezekowitz, M.E. Field, K.T. Murray, R.L. Sacco, W.G. Stevenson, P.J.
563 Tchou, C.M. Tracy, C.W. Yancy, J.L. Anderson, J.L. Halperin, N.M. Albert, B. Bozkurt, R.G.
564 Brindis, M.A. Creager, L.H. Curtis, D. Demets, R.A. Guyton, J.S. Hochman, R.J. Kovacs,
565 E.M. Ohman, S.J. Pressler, F.W. Sellke, W. Shen, W.G. Stevenson, C.W. Yancy, 2014 AHA
566 / ACC / HRS Guideline for the Management of Patients With Atrial Fibrillation. A Report
567 of the American College of Cardiology / American Heart Association Task Force on
568 Practice Guidelines and the Heart Rhythm Society, 2014.
569 doi:10.1161/CIR.0000000000000041.

570 [4] G.A. Roth, C. Johnson, A. Abajobir, F. Abd-allah, S.F. Abera, C. Ms, G. Abyu, M. Ahmed,
571 B. Aksut, T. Alam, J. Ärnlöv, H. Asayesh, M. Atey, C. Ms, L. Avila-burgos, A. Awasthi, C.
572 Ms, A. Banerjee, D.P. Hil, A. Barac, T. Bärnighausen, L. Barregard, N. Bedi, S. Bitew, J.
573 Carapetis, J. Carrero, C.A. Castañeda-orjuela, C. Ms, J. Castillo-rivas, F. Catalá-lópez, J.
574 Choi, H. Christensen, I. Dmsc, M. Cirillo, L. Cooper, M. Criqui, D. Cundiff, A. Damasceno,
575 L. Dandona, R. Dandona, K. Davletov, S. Dharmaratne, M. Farvid, V. Feigin, E.L. Ding, G.

576 Fowkes, T. Gebrehiwot, R. Gillum, A. Gold, C. Ms, P. Gona, R. Gupta, T.D. Habtewold, C.
577 Ms, N. Hafezi-nejad, T. Hailu, B. Hailu, C. Ms, S. James, M. Javanbakht, P. Jeemon, D.
578 John, J. Jonas, Y. Kalkonde, C. Karimkhani, A. Kasaeian, Y. Khader, A. Khan, Y. Khang, S.
579 Khera, A.T. Khoja, K.J. Krohn, G.A. Kumar, G.F. Kwan, K. Lal, A. Larsson, S. Linn, D.R. Ph,
580 A. Lopez, P.A. Lotufo, D.R. Ph, M. Abd, E. Razek, H. Mbbc, R. Malekzadeh, M. Mazidi, T.
581 Meier, G. Meles, G. Mensah, A. Meretoja, H. Mezgebe, C. Ms, T. Miller, E. Mirrakhimov,
582 A.E. Moran, I. Musa, J. Narula, M. Owolabi, C. Ms, D.M. Ed, G. Patton, J. Pedro, D. Qato,
583 P.D. Harm, C.S. Wiysonge, C. Wolfe, A. Workicho, G. Xu, Global , Regional , and National
584 Burden of Cardiovascular Diseases for 10 Causes , 1990 to 2015, J. Am. Coll. Cardiol. 70
585 (2017) 1–25. doi:10.1016/j.jacc.2017.04.052.

586 [5] P. Kirchhof, S. Benussi, D. Kotecha, A. Ahlsson, D. Atar, B. Casadei, M. Castella, H.-C.
587 Diener, H. Heidbuchel, J. Hendriks, G. Hindricks, 2016 ESC Guidelines for the
588 management of atrial fibrillation developed in collaboration with EACTS, Eur. Heart J.
589 (2016). doi:10.1093/eurheartj/ehw210.

590 [6] L. Mont, F. Bisbal, N. Hernández-Madrid, APérez-Castellano, X. Viñolas, A. Arenal, F.
591 Arribas, I. Fernández-Lozano, A. Bodegas, J. Pérez-Villacastín, J.M. Guerra, P. Ávila, M.
592 López-Gil, V. Castro, J.I. Arana, J. Brugada, Catheter ablation vs. antiarrhythmic drug
593 treatment of persistent atrial fibrillation: a multicentre, randomized, controlled trial
594 (SARAstudy), Eur. Heart J. 35 (2014) 501–507.

595 [7] L. Shi, R. Heng, S. Liu, F. Leng, Effect of catheter ablation versus antiarrhythmic drugs on
596 atrial fibrillation: A meta-analysis of randomized controlled trials., Exp. Ther. Med. 10
597 (2015) 816–822.

598 [8] A. Hakalahti, F. Biancari, J.C. Nielsen, M.J.P. Raatikainen, Radiofrequency ablation vs.
599 antiarrhythmic drug therapy as first line treatment of symptomatic atrial fibrillation:

systematic review and metaanalysis, Europace. 17 (2015) 370–378.

[9] M. Haïssaguerre, P. Jaïs, D.C. Shah, a Takahashi, M. Hocini, G. Quiniou, S. Garrigue, a Le Mouroux, P. Le Métayer, J. Clémenty, Spontaneous initiation of atrial fibrillation by ectopic beats originating in the pulmonary veins., N. Engl. J. Med. 339 (1998) 659–666. doi:10.1097/00045415-199903000-00006.

[10] C. Pappone, G. Oreto, S. Rosanio, G. Vicedomini, M. Tocchi, F. Gugliotta, A. Salvati, C. Dicandia, M.P. Calabrò, P. Mazzone, E. Ficarra, C. Di Gioia, S. Gulletta, S. Nardi, V. Santinelli, S. Benussi, O. Alfieri, Atrial Electroanatomic Remodeling After Circumferential Raiofrequency Pulmonary Vein Ablation. Efficacy of an Anatomic Approach in a Large Cohort of Patients with Atria Fibrillation, Circulation. 104 (2001) 2539–2545.

[11] H. Oral, B.P. Knight, H. Tada, M. Özaydın, A. Chugh, S. Hassan, C. Scharf, S.W.K. Lai, R. Greenstein, F.J. Pelosi, S.A. Strickberger, F. Morady, Pulmonary Vein Isolation for Paroxysmal and Persistent Atrial Fibrillation, Circulation. 105 (2002) 1077–1081. doi:10.1161/hc0902.104712.

[12] D.M. Todd, A.C. Skanes, G. Guiraudon, C. Guiraudon, A.D. Krahn, R. Yee, G.J. Klein, Role of the Posterior Left Atrium and Pulmonary Veins in Human Lone Atrial Fibrillation, Circulation. 108 (2003) 3108–3114. doi:10.1161/01.CIR.0000104567.72914.BF.

[13] R. Mandapati, a Skanes, J. Chen, O. Berenfeld, J. Jalife, Stable microreentrant sources as a mechanism of atrial fibrillation in the isolated sheep heart., Circulation. 101 (2000) 194–199. doi:10.1161/01.CIR.101.2.194.

[14] M. Yamazaki, S. Mironov, C. Taravant, J. Brec, L.M. Vaquero, K. Bandaru, U.M.R. Avula, H. Honjo, I. Kodama, O. Berenfeld, J. Kalifa, Heterogeneous atrial wall thickness and stretch promote scroll waves anchoring during atrial fibrillation, Cardiovasc. Res. 94

623 (2012) 48–57. doi:10.1093/cvr/cvr357.

624 [15] M. Mansour, R. Mandapati, O. Berenfeld, J. Chen, F.H. Samie, J. Jalife, Left-to-right
625 gradient of atrial frequencies during acute atrial fibrillation in the isolated sheep heart.,
626 Circulation. 103 (2001) 2631–2636. doi:10.1161/01.CIR.103.21.2631.

627 [16] O. Berenfeld, A. V. Zaitsev, S.F. Mironov, A.M. Pertsov, J. Jalife, Frequency-dependent
628 breakdown of wave propagation into fibrillatory conduction across the pectinate
629 muscle network in the isolated sheep right atrium, Circ. Res. 90 (2002) 1173–1180.
630 doi:10.1161/01.RES.0000022854.95998.5C.

631 [17] B.J. Hansen, J. Zhao, T.A. Csepe, B.T. Moore, N. Li, L.A. Jayne, A. Kalyanasundaram, P.
632 Lim, A. Bratasz, K.A. Powell, O.P. Simonetti, R.S.D. Higgins, A. Kilic, P.J. Mohler, P.M.L.
633 Janssen, R. Weiss, J.D. Hummel, V. V. Fedorov, Atrial fibrillation driven by micro-
634 anatomic intramural re-entry revealed by simultaneous sub-epicardial and sub-
635 endocardial optical mapping in explanted human hearts, Eur. Heart J. 36 (2015) 2390–
636 2401. doi:10.1093/eurheartj/ehv233.

637 [18] J. Zhao, B.. Hansen, Y. Wang, T.. Csepe, L.. Sul, A. Tang, Y. Yuan, N. Li, A. Bratasz, K..
638 Powell, A. Kilic, P.. Mohler, P.. Janssen, R. Weiss, O.. Simonetti, J.. Hummel, V.. Fedorov,
639 Three-dimensional Integrated Functional, Structural, and Computational Mapping to
640 Define the Structural ”Fingerprints” of Heart-Specific Atrial Fibrillation Drivers in Human
641 Heart Ex Vivo, J. Am. Heart Assoc. 6 (2017) e005922.

642 [19] S.M. Narayan, D.E. Krummen, M.W. Enyeart, W.J. Rappel, Computational Mapping
643 Identifies Localized Mechanisms for Ablation of Atrial Fibrillation, PLoS One. 7 (2012) 1–
644 8. doi:10.1371/journal.pone.0046034.

645 [20] S.M. Narayan, K. Shivkumar, D.E. Krummen, J.M. Miller, W.-J. Rappel, Panoramic

646 Electrophysiological Mapping but not Electrogram Morphology Identifies Stable Sources
647 for Human Atrial Fibrillation. Stable Atrial Fibrillation Rotors and Focal Sources Relate
648 Poorly to Fractionated Electrograms, Circ. Arrhythmia Electrophysiol. 6 (2013) 58–67.
649 doi:10.1161/CIRCEP.111.977264.

650 [21] S.M. Narayan, D.E. Krummen, K. Shivkumar, P. Clopton, W.J. Rappel, J.M. Miller,
651 Treatment of atrial fibrillation by the ablation of localized sources: CONFIRM
652 (Conventional Ablation for Atrial Fibrillation with or Without Focal Impulse and Rotor
653 Modulation) trial, J. Am. Coll. Cardiol. 60 (2012) 628–636.
654 doi:10.1016/j.jacc.2012.05.022.

655 [22] W.J. Rappel, S.M. Narayan, Theoretical considerations for mapping activation in human
656 cardiac fibrillation, Chaos. 23 (2013). doi:10.1063/1.4807098.

657 [23] T. Yamada, Pulmonary vein isolation with a multielectrode basket catheter, Indian
658 Pacing Electrophysiol. J. 7 (2007) 97–109.

659 [24] P. Benharash, E. Buch, P. Frank, M. Share, R. Tung, K. Shivkumar, R. Mandapati,
660 Quantitative Analysis of Localized Sources Identified by Focal Impulse and Roter
661 Modulation Mapping in Atrial Fibrillation, Circ. Arrhythmia Electrophysiol. 8 (2015) 554–
662 61. doi:10.1161/CIRCEP.115.002721.

663 [25] N. Sasaki, Y. Okumura, I. Watanabe, K. Nagashima, K. Takahashi, K. Iso, Localized rotors
664 and focal impulse sources within the left atrium in human atrial fi brillation : A phase
665 analysis of contact basket catheter electrograms, J. Arrhythmia. 32 (2016) 141–144.
666 doi:10.1016/j.joa.2015.11.010.

667 [26] C.-T. Tai, S.-A. Chen, Noncontact Mapping of the Heart : How and When to Use, J.
668 Cardiovasc. Electrophysiol. 20 (2009) 123–126. doi:10.1111/j.1540-8167.2008.01302.x.

669 [27] J.L. Salinet, N. Masca, P.J. Stafford, G.A. Ng, F.S. Schlindwein, Three - dimensional
670 dominant frequency mapping using autoregressive spectral analysis of atrial
671 electrograms of patients in persistent atrial fibrillation, Biomed. Eng. Online. (2016) 1–
672 15. doi:10.1186/s12938-016-0143-8.

673 [28] R. Weerasooriya, P. Khairy, J. Litalien, L. Macle, M. Hocini, F. Sacher, N. Lellouche, S.
674 Knecht, M. Wright, I. Nault, S. Miyazaki, C. Scavee, J. Clementy, M. Haissaguerre, P. Jais,
675 Catheter Ablation for Atrial Fibrillation. Are Results Maintained at 5 Years of Follow-
676 Up ?, JACC. 57 (2011) 160–166. doi:10.1016/j.jacc.2010.05.061.

677 [29] E. Buch, M. Share, R. Tung, P. Sharma, J. Koneru, R. Mandapati, K.A. Ellenbogen, K.
678 Shivkumar, L. Angeles, L. Linda, Long-term clinical outcomes of focal impulse and rotor
679 modulation for treatment of atrial fibrillation: A multicenter experience, Hear. Rhythm.
680 13 (2016) 636–641. doi:10.1016/j.hrthm.2015.10.031.

681 [30] R.F. Berntsen, T.F. Håland, R. Skårdal, T. Holm, Focal impulse and rotor modulation as a
682 stand-alone procedure for the treatment of paroxysmal atrial fi brillation : A within-
683 patient controlled study with implanted cardiac monitoring, Hear. Rhythm. 22 (2016) 1–
684 7. doi:10.1016/j.hrthm.2016.04.016.

685 [31] J. Jalife, D. Filgueiras-Rama, O. Berenfeld, Letter by Jalife et al Regarding Article,
686 “Quantitative Analysis of Localized Sources Identified by Focal Impulse and Rotor
687 Modulation Mapping in Atrial Fibrillation,” 8 (2015) 1296–1298. doi:10.1038/32164.2.

688 [32] S.M. Narayan, J. Jalife, CrossTalk proposal: Rotors have been demonstrated to drive
689 human atrial fibrillation., J. Physiol. 592 (2014) 3163–3166.
690 doi:10.1113/jphysiol.2014.271031.

691 [33] M. Allessie, N. De Groot, CrossTalk opposing view: Rotors have not been demonstrated

692 to be the drivers of atrial fibrillation, Physiol, J. 592 (2014) 3167–3170.
693 doi:10.1113/jphysiol.2014.271809.

694 [34] S.M. Narayan, J. Jalife, Rebuttal from Sanjiv M. Narayan and Jose Jalife, J. Physiol. 592
695 (2014) 3171–3171. doi:10.1113/jphysiol.2014.275396.

696 [35] M. Allessie, N. De Groot, Rebuttal from Maurits Allessie and Natasja de Groot, J Physiol.
697 592 (2014) 3173. doi:10.1113/jphysiol.2014.275404.

698 [36] L. Martinez-Mateu, L. Romero, A. Ferrer-Albero, R. Sebastian, J.F. Rodríguez Matas, J.
699 Jalife, O. Berenfeld, J. Saiz, Factors affecting basket catheter detection of real and
700 phantom rotors in the atria: A computational study, PLoS Comput. Biol. (2018).
701 doi:10.1371/journal.pcbi.1006017.

702 [37] J.M. Miller, R.C. Kowal, V. Swarup, J.P. Daubert, E.G. Daoud, J.D. Day, K. a. Ellenbogen,
703 J.D. Hummel, T. Baykaner, D.E. Krummen, S.M. Narayan, V.Y. Reddy, K. Shivkumar, J.S.
704 Steinberg, K.R. Wheelan, Initial Independent Outcomes from Focal Impulse and Rotor
705 Modulation Ablation for Atrial Fibrillation: Multicenter FIRM Registry, J. Cardiovasc.
706 Electrophysiol. (2014) 921–929. doi:10.1111/jce.12474.

707 [38] J. Laughner, S. Shome, N. Child, A. Shuros, P. Neuzil, J. Gill, M. Wright, Practical
708 considerations of mapping persistent atrial fibrillation with whole-chamber basket
709 catheters, JACC Clin. Electrophysiol. 2 (2016) 55–65. doi:10.1016/j.jacep.2015.09.017.

710 [39] L. Martínez, J. Jalife, O. Berenfeld, J. Saiz, Are Multi-electrode Arrays able to
711 Differentiate Anatomical from Functional Reentries in an Excitable Sheet?, in: Comput.
712 Cardiol. (2010)., 2015: pp. 865–868.

713 [40] M. Courtemanche, R.J. Ramirez, S. Nattel, Ionic mechanisms underlying human atrial
714 action potential properties: insights from a mathematical model, Am J Physiol Hear. Circ

715 Physiol. 275 (1998) 301–321.

716 [41] E.A. Heidenreich, J.M. Ferrero, M. Doblaré, J.F. Rodríguez, Adaptive macro finite
717 elements for the numerical solution of monodomain equations in cardiac
718 electrophysiology, Ann. Biomed. Eng. 38 (2010) 2331–2345. doi:10.1007/s10439-010-
719 9997-2.

720 [42] D.U.J. Keller, F.M. Weber, G. Seemann, O. Dössel, Ranking the influence of tissue
721 conductivities on forward-calculated ecgs, IEEE Trans. Biomed. Eng. 57 (2010) 1568–
722 1576. doi:10.1109/TBME.2010.2046485.

723 [43] D.B. Geselowitz, W. Miller, A BIDOMAIN MODEL FOR ANISOTROPIC CARDIAC MUSCLE,
724 Ann. Biomed. Eng. 11 (1983) 191–206.

725 [44] M. Yamazaki, D. Filgueiras-Rama, O. Berenfeld, J. Kalifa, Ectopic and reentrant
726 activation patterns in the posterior left atrium during stretch-related atrial fibrillation,
727 Prog. Biophys. Mol. Biol. 110 (2012) 269–277. doi:10.1016/j.pbiomolbio.2012.08.004.

728 [45] M. Warren, P.K. Guha, O. Berenfeld, A. Zaitsev, J.M.B. Anumonwo, A.S. Dhamoon, S.
729 Bagwe, S.M. Taffet, J. Jalife, Blockade of the inward rectifying potassium current
730 terminates ventricular fibrillation in the guinea pig heart, J. Cardiovasc. Electrophysiol.
731 14 (2003) 621–631. doi:10.1046/j.1540-8167.2003.03006.x.

732 [46] R. Gray, A. Pertsov, J. Jalife, Spatial and temporal organization during cardiac fibrillation,
733 Nature. 392 (1998) 75–78. doi:10.1107/S0108768196005599.

734 [47] J. Chen, R. Mandapati, O. Berenfeld, A.C. Skanes, High-Frequency Periodic Sources
735 Underlie Ventricular Fibrillation in the Isolated Rabbit Heart, Circ. Res. 86 (2000) 86–93.

736 [48] N.D. Mermin, The topological theory of defects in ordered media, Rev. Mod. Phys. 51
737 (1979) 591–648. doi:10.1103/RevModPhys.51.591.

738 [49] A. Goryachev, R. Kapral, Spiral waves in chaotic systems., Phys. Rev. Lett. 76 (1996)
739 1619–1622. http://www.ncbi.nlm.nih.gov/pubmed/10060475.

740 [50] J.M. Rogers, Combined Phase Singularity and Wavefront Analysis for Optical Maps of
741 Ventricular Fibrillation, IEEE Trans. Biomed. Eng. 51 (2004) 56–65.
742 doi:10.1109/TBME.2003.820341.

743 [51] M. Rodrigo, M.S. Guillem, A.M. Climent, J. Pedron-Torrecilla, A. Liberos, J. Millet, F.
744 Fernandez-Aviles, F. Atienza, O. Berenfeld, Body surface localization of left and right
745 atrial high-frequency rotors in atrial fibrillation patients: A clinical-computational study,
746 Hear. Rhythm. 11 (2014) 1584–1591. doi:10.1016/j.hrthm.2014.05.013.

747 [52] J.W. Waks, M.E. Josephson, Mechanisms of Atrial Fibrillation – Reentry, Rotors and
748 Reality, Arrhythmia Electrophysiol. Rev. 3 (2014) 90–100.

749 [53] C. Roney, C. Cantwell, J. Bayer, N. Qureshi, P. Lim, J. Tweedy, Spatial Resolution
750 Requirements for Accurate Identification of Drivers of Atrial Fibrillation, Circ Arrhythmia
751 Electrophysiol. (2017) 1–13.

752 [54] J.M. Miller, G.S. Tyson, W.C. Hargrove, J.A. Vassallo, M.E. Rosenthal, M.E. Josephson,
753 Effect of subendocardial resection on sinus rhythm endocardial electrogram
754 abnormalities, Circulation. 91 (1995) 2385–91.

755 [55] E. Anter, M.E. Josephson, Bipolar voltage amplitude: What does it really mean?, Hear.
756 Rhythm. 13 (2016) 326–327. doi:10.1016/j.hrthm.2015.09.033.

757 [56] O. Berenfeld, H. Oral, The Quest for Rotors in Atrial fibrillation: Different Nets Catch
758 Different Fishes, Hear. Rhythm. 9 (2012) 1440–1441.

759 [57] Z. Ling, J. Mcmanigle, V. Zipunnikov, F. Pashakhanloo, I.M. Khurram, S.L. Zimmerman, B.
760 Philips, J.E. Marine, D.D. Spragg, A. Hiroshi, H. Calkins, S. Nazarian, The association of

761 left atrial low voltage regions on electroanatomic mapping with low attenuation regions
762 on cardiac computed tomography perfusion imaging in patients with atrial fibrillation,
763 12 (2015) 857–864. doi:10.1016/j.hrthm.2015.01.015.The.

764 [58] E. Anter, C.M. Tschabrunn, A.E. Buxton, M.E. Josephson, High-Resolution Mapping of
765 Post-Infarction Reentrant Ventricular Tachycardia: Electrophysiological Characterization
766 of the Circuit, Circulation. 134 (2016) 314–327.

767 [59] J.M. Davidenko, A. V. Pertsov, R. Salomonsz, W. Baxter, J. Jalife, Stationary and drifting
768 spiral waves of excitation in isolated cardiac muscle, Nature. 355 (1992) 349–351.

769 [60] R. Tung, M.E. Josephson, J.S. Bradfield, K. Shivkumar, Directional Influences of
770 Ventricular Activation on Myocardial Scar Characterization: Voltage Mapping with
771 Multiple Wavefronts during Ventricular Tachycardia Ablation, Circ. Arrhythmia
772 Electrophysiol. 9 (2016) 1–11. doi:10.1161/CIRCEP.116.004155.

773 [61] I.R. Efimov, V.P. Nikolski, G. Salama, Optical imaging of the heart, Circ. Res. 95 (2004)
774 21–33. doi:10.1161/01.RES.0000130529.18016.35.

775